RAS Techniques and Instruments

RASTAI **2,** 723–734 (2023) https://doi.org/10.1093/rasti/rzad047
Advance Access publication 2023 October 16

Experimental and analytical methods for thermal infrared spectroscopy of complex dust coatings in a simulated asteroid environment

C. R. Tinker ,[1]★ T. D. Glotch,[1] L. B. Breitenfeld,[1] A. Ryan[2] and L. Li[1]

[1] *Center for Planetary Exploration, Stony Brook University, Stony Brook, NY 11794, USA*
[2] *Lunar and Planetary Laboratory, University of Arizona, Tucson, AZ 85721, USA*

Accepted 2023 September 25. Received 2023 August 29; in original form 2023 April 12

ABSTRACT

Airless bodies in the Solar system are commonly dominated by complex regolith mixtures consisting of coarse and fine particulates. These materials often manifest as coatings with the potential to modify or obscure the spectral signatures of underlying substrates. This can make accurate spectral analysis of surface materials challenging, especially for thermal infrared (TIR) techniques of which the spectral properties concurrently depend on grain size and albedo. Further complexity is presented when these coatings occur as discontinuous patterns in which some substrate is exposed and some is masked. Discontinuous patterns are distinguished by scale as having macroscopic or microscopic discontinuity, with the former being patches of homogeneous dust covering portions of the substrate and the latter being randomly distributed individual particles on the substrate. Investigations of asteroid (101955) Bennu's surface by NASA's Origins, Spectral Interpretation, Resource Identification, and Security-Regolith Explorer have revealed contradictions between spectral and thermophysical results that are hypothesized to indicate the presence of thin and/or laterally discontinuous dust coatings. To address this, we constructed an environment chamber that enables the controlled deposition of size-regulated dust particles in coatings with varying continuity and thickness. TIR spectra of coated substrates acquired in a simulated asteroid environment are used to investigate the extent to which dust coatings of different thicknesses and arrangements contribute to orbital spectral signatures of airless body surfaces.

Key words: Instrumentation – Spectroscopy – Simulated Asteroid Environment – (101955) Bennu.

1. INTRODUCTION

Thermal inertia can be viewed as a measure of a material's ability to conduct heat to its surroundings, or its resistance to change in temperature. The thermal inertia of airless bodies is controlled by the thermophysical properties of the surface, including thermal conductivity and volumetric heat capacity. A common practice is to interpret thermal inertia values in terms of a characteristic regolith particle size, as it is known to strongly affect thermal conductivity on airless bodies (Gundlach & Blum 2013; Emery et al. 2014; MacLennan & Emery 2022). Telescopic observations of Bennu by the *Spitzer Space Telescope* yielded a disc-averaged thermal inertia of 310 ± 70 J m^{-2} K^{-1} s$^{-1/2}$, consistent with the presence of broad-scale millimetre- to centimetre-scale particulates covering the surface. Contrary to these expectations, images of Bennu returned by NASA's Origins, Spectral Interpretation, Resource Identification, and Security-Regolith Explorer (OSIRIS-REx) appeared to lack abundant fines and instead were dominated by decametre-scale boulders (DellaGiustina et al. 2019; Lauretta et al. 2019). The lowest thermal inertia values across Bennu's surface are associated with the largest boulders, while regions lacking very large boulders but containing abundant smaller, higher albedo boulders with higher inferred density and thermal conductivity have a higher than average thermal inertia (DellaGiustina et al. 2019; Rozitis et al. 2019, 2020). DellaGiustina et al. (2019) proposed that the low thermal inertia of Bennu's boulders may be explained by local dust cover, which is supported by the association of transparency features (TFs) in thermal infrared (TIR) spectra attributable to dust with regions dominated by rough, dark boulders (DellaGiustina et al. 2019; Hamilton et al. 2019, 2021; Rozitis et al. 2020). This is contradicted by thermal model results that can provide accurate fits to the OSIRIS-REx Thermal Emission Spectrometer (OTES) data while assuming a constant thermal inertia with depth (Rozitis et al. 2019, 2020). Additional models show that continuous dust layers as thin as 10–100 μm can distort diurnal temperature curves in a way that is inconsistent with the OTES observations (Biele et al. 2019). However, thin and heterogeneous dust coatings could contribute to a lower thermal inertia of boulders without significantly distorting diurnal temperature curves in the manner discussed by Biele et al. (2019). Dust-free thermal models of Bennu fit best with OTES data; however, thin dust coatings (<50 μm) with low spatial coverage (5–10 per cent) cannot be ruled out as they produce an acceptable fit to the observations. Thermal models for discontinuous dust coatings fit to OSIRIS-REx Visible and Infrared Spectrometer data show similar results with fit quality decreasing as the dust fraction increases (Rozitis et al. 2020). These models demonstrate that thick continuous dust layers (>50 μm) on Bennu's boulders would not produce diurnal brightness temperature curves consistent with the observed data. Furthermore, thermal models of thin dust coatings are relatively

★ E-mail: connor.tinker@stonybrook.edu

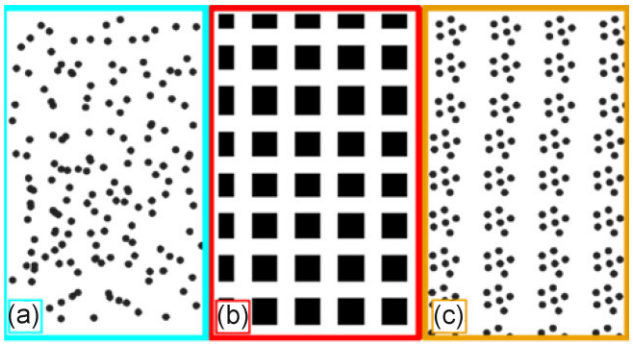

Figure 1. Three different forms of dust coating discontinuity expected in laboratory and orbital contexts: (a) micro-discontinuous (MiD), (b) arranged macro-discontinuous, and (c) mixed-discontinuous.

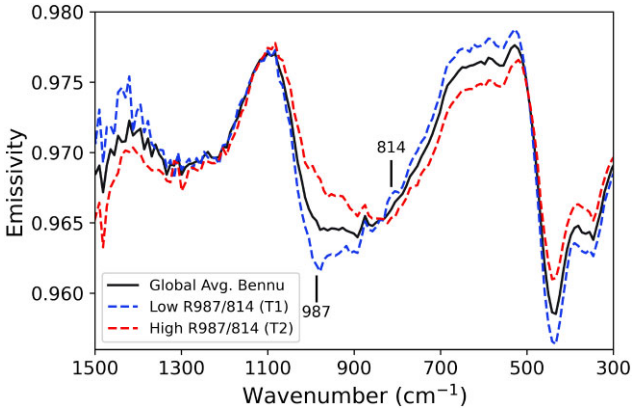

Figure 2. OTES global average spectrum of Bennu and two spectral indices defined by Hamilton et al. (2021) for the lowest and highest R987/814 cm^{-1} ratio values in 100 EQ3 (12:30 pm) Detailed Survey station spectra. T2 is shown in red and exhibits the highest average R987/814 values. These indices quantify variability between T1 and T2 and highlight where they are most distinct.

immature. They rely on the assumption that the dust coating is completely opaque at visible and thermal wavelengths, such that no solar insolation or thermal emission penetrates through the upper or lower boundaries of the dust layer. A physically realistic dust layer is expected to transmit some fraction of visible and thermal radiance, thus diminishing its insulating properties compared with standard opaque model assumption. The effect is that the opaque model predictions for maximum feasible dust thickness may be underestimates. That is to say that the diurnal brightness temperature data from OTES may actually be consistent with somewhat thicker dust coatings than stated in Rozitis et al. (2020).

To reconcile the discrepancy between the OTES spectra and thermal model results, we need to constrain the spectral effects of dust coatings and link them to bulk thermophysical properties in a controlled laboratory setting. By doing so, we can estimate the physical properties of Bennu's surface by connecting orbital spectral data to consistent thermal models based on correlations established in the lab. There is no fully relevant laboratory study that has characterized the spectral and thermophysical effects of dust across a variety of coating thicknesses and continuity patterns. Dust coating continuity can be characterized by scale as having macroscopic or microscopic discontinuity, with the former being patches of homogeneous dust covering portions of the substrate and the latter being randomly distributed individual particles on the substrate (Fig. 1). The global average TIR spectrum of Bennu from OTES does not perfectly match any single carbonaceous chondrite (CC) but has individual features similar to a variety of known samples (Hamilton et al. 2019, 2021). OTES spectra exhibit a Christiansen feature (CF, ~1090 cm^{-1}) most similar to that for CM1/2 and CM2 petrologic types. A broad silicate stretching feature between ~1090 and 650 cm^{-1} is most similar to that observed in CI Chondrites, such as Orgueil, and band minima at 440 cm^{-1} predominantly attributed to silicate bending modes that are very similar to that observed in CI and CM CC groups. Minor features at 555 and 340 cm^{-1} are, in part, a result of volumetrically abundant magnetite (Hamilton et al. 2019). Partial least squares machine learning models of OTES data predict that Bennu's average global composition is 78 per cent phyllosilicates, 9 per cent olivine, 11 per cent carbonates, and 6 per cent magnetite (Breitenfeld et al. 2021). Bennu's composition is most consistent with aqueously altered CI/CM chondrites as it is dominated by phyllosilicates and contains <10 volume per cent anhydrous silicates. The OTES Detailed Survey Equatorial 3 (EQ3) station observations have a nadir spatial resolution of 1255 m^2 (40 m per spectrum, excluding smear) and were acquired at greater mean emission angles of 7–69°. EQ3 data were collected at a local time of 12:30 pm, reducing the amount of equatorial shadowing while offering the highest surface temperatures and best signal-to-noise ratio. Nearly all OTES spectra can be modelled as a linear combination of two end-member spectra (Fig. 2) which are most distinct between ~1000 and 800 cm^{-1}. Spectral indices are correlated with visible albedo and thermal inertia, with T1 being abundant across the surface and T2 corresponding to large (≥ 20 m), rough, dark boulders with low thermal inertias (DellaGiustina et al. 2020; Rozitis et al. 2020; Hamilton et al. 2021). T1 may indicate a higher proportion of rocks and regolith particles much larger than the wavelength of light (~10 μm), while T2 likely has a larger abundance of fine particulates. Differences between T1 and T2 spectral indices may result from the presence of fine particulates (<10 μm) associated with T2 that introduce weak volume scattering while reducing the contrast of silicate Reststrahlen bands (RBs, Aronson & Emslie 1973; Salisbury & Eastes 1985; Salisbury & Walter 1989; Moersch & Christensen 1995; Mustard & Hays 1997; Ramsey & Christensen 1998; Pan, Rogers & Thorpe 2015; Thorpe et al. 2015; Hardgrove et al. 2016; Hamilton et al. 2021). OTES spectra do not exhibit features indicative of deposits volumetrically dominated by fine particulates including strong TF and a CF shifted to shorter wavelengths (Salisbury, D'Aria & Jarosewich 1991; Hamilton et al. 2021). When comparing T2 with T1 and considering adjustments for emissivity differences due to changes in the RB, T2 shows evidence of weak TF near ~822 cm^{-1}. T1-dominated spectra also exhibit a very small proportion of fines as indicated by a spectral slope >1090 cm^{-1} and potentially the peak at 1420 cm^{-1} (Hamilton et al. 2021). While not indicative of extensive, thick dust deposits, these spectral effects correspond to observations in laboratory experiments involving thin dust coatings on both particulate and solid surfaces at ambient and Mars pressures (Johnson, Christensen & Lucey 2002; Graff 2003; Rivera-Hernandez et al. 2015; Hamilton et al. 2021). Hamilton et al. (2021) hypothesized that the association of spectral features attributable to dust with Bennu's rough, dark boulders may indicate the production and/or trapping of fines in coatings on boulders. Local dust deposits are consistent with alternative thermal models that limit coatings to be <50 μm whether or not they are laterally continuous (Rozitis et al. 2020). These results show that thermal models attempting to characterize the surface of airless bodies may need to account for thin, porous, and/or laterally discontinuous dust coatings.

Addressing the inconsistencies apparent in the OSIRIS-REx spectral and thermophysical observations requires paired spectral and thermophysical analyses of simple and complex dust coatings in a controlled, relevant environment. TIR spectra of dust coatings with varying thicknesses and porosities will help determine at which point substrates become obscured, and when dust can be considered optically thick. Orbital observations are large enough in scale that they are rarely entirely obscured by dust, and coatings instead appear in a macro-discontinuous and/or MiD pattern. A survey of coating continuity and coverage will show how discontinuous dust patterns are spectrally different from homogeneous coatings. These results will also demonstrate the relative contribution substrates and the coated dust have at different bands in the spectra. These spectral results can be combined with thermal models to determine how vertical and lateral temperature variations within dust layers affect the apparent thermal inertia. This paper describes the design, construction, and calibration of a custom dust deposition chamber capable of creating constrained coated samples with controlled or measurable particle size, thickness, porosity, and continuity. A set of test coatings are used to characterize the reliability of the deposition cycle and provide preliminary spectral results that allow for informed adjustment of the independent variables to elicit a measurable response.

2. FACTORS AFFECTING TIR SPECTROSCOPY IN AIRLESS BODY ENVIRONMENTS

Environmental conditions, particle size, and albedo have complex and interconnected effects on TIR spectroscopy. Under airless body conditions, surface regolith absorbs solar radiation and is heated to a greater depth than the thickness of the infrared emitting layer. This results in a layered thermal structure with a cold thin surface and warm interior (Logan & Hunt 1970; Logan et al. 1973; Salisbury & Walter 1989). Radiance in the RB region (8–12 μm) stems from the shallow, cool surface, while that from the CF originates from the deeper and hotter subsurface (Nash et al. 1993). Absorption is more efficient in the RB region, meaning radiation from the shallow (micron scale) surface tends to dominate emission. Previous studies measuring the effects of decreased pressure ($<10^{-4}$ mbar) in a simulated asteroid environment (SAE) on TIR spectroscopy of fine particulates have shown that spectral contrast increases, and increased absorption in the RB region causes shifts in the CF to shorter wavelengths (Logan et al. 1973; Salisbury & Walter 1989; Henderson, Lucey & Jakosky 1996; Donaldson Hanna et al. 2014, 2017, 2019; Shirley & Glotch 2019).

Bennu has a relatively low visible albedo (∼0.04) which contributes to a reduced thermal gradient in the regolith when compared with the Moon (Lauretta et al. 2019). As shown in Fig. 3a, decreasing albedo results in a lower frequency CF (Fig. 3b) and an increase in the minimum emissivity of the RB (Fig. 3c). Expected reductions in overall spectral contrast because of darkening are accompanied by changes in the RB shape; therefore, changes in contrast due to albedo cannot be modelled by the simple addition of a blackbody component (Fig. 3d). Reductions in albedo tend to reduce spectral differences between ambient and SAE spectra; however, darkened SAE spectra have a significantly reduced TF, shallower silicate 'roll-off' slope shortward of the CF, and a CF position shifted to higher frequencies compared with ambient counterparts (Glotch, Shirley & Greenhagen 2017; Breitenfeld et al. 2019; Shirley & Glotch 2019). These interconnected effects demonstrate the need to account for albedo and environmental conditions concurrently in any study focused on Bennu and other dark airless bodies.

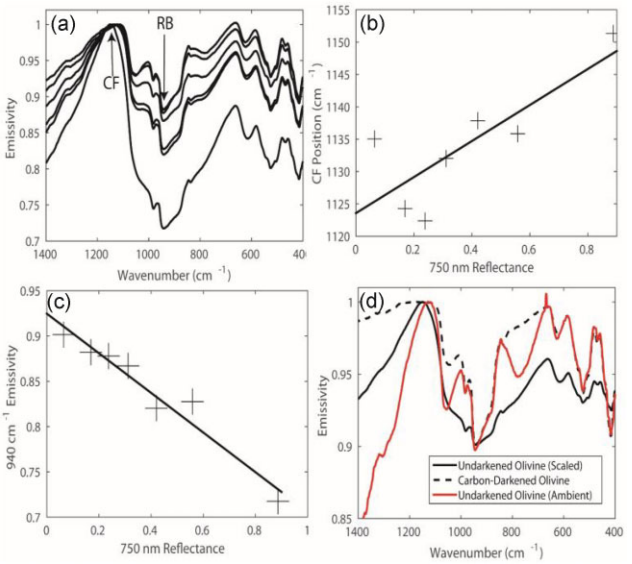

Figure 3. (a) SAE spectra of darkened olivine (<63 μm particle size fraction). (b) Decreasing albedo (reflectance at 750 nm) results in shift of the CF to lower frequencies. (c) Decreasing albedo (reflectance at 750 nm) reduces spectral contrast and increases emissivity in RB. (d) SAE TIR spectra of carbon-darkened olivine (dashed line) compared with undarkened olivine scaled (solid line) through the addition of a blackbody component. TIR spectral contrast changes due to darkening cannot be easily modelled through addition of a blackbody component and do not resemble spectra of the same material acquired under ambient conditions (shown in red).

Shirley & Glotch (2019) demonstrated that in airless body environments decreasing particle size results in a stronger RB and TF. Increased volume scattering effects drive emissivity down shortward of the silicate CF, a trend that is opposite of what is typically observed under ambient conditions. Glotch et al. (2018) demonstrated the effects of particle size in an SAE for low albedo (∼0.04) carbonate-poor material from the C2-ungrouped meteorite Tagish Lake. The chip spectrum has the most spectral contrast, while the coarse particulate spectrum has the least. The coarse particulate exhibits a CF shift towards longer wavelengths and a slight decrease in emissivity shortward of the CF. The fine particulate exhibits a further shift of the CF towards longer wavelengths and additional reduction in emissivity shortward of the CF. These studies investigated chip, fine, and coarse samples individually, which may not accurately represent regolith mixtures found on airless bodies.

Crisp & Bartholomew (1992), Graff, Morris & Christensen (2001), Johnson et al. (2002), and Graff (2003) used biconical reflectance or thermal emission spectroscopy to study the effects of dust coatings on TIR spectra under ambient conditions. These studies showed that the RB becomes shallower and emissivity decreases shortward of the CF with increasing dust coating thickness. Johnson et al. (2002) demonstrated strong reductions in RB strength with coatings as thin as ∼20 μm and showed that coatings ∼100 μm thick can entirely dominate the spectra. Rivera-Hernandez et al. (2015) combined TIR spectroscopic laboratory measurements with radiative transfer (RT) modelling to quantify spectral contributions produced by optically thin dust coatings under Mars environmental conditions (∼360 K, ∼6.5 mbar). Their study showed that optically thin surface dust did not block substrate emittance, and instead acted as an absorber and emitter, contributing spectral features at specific bands where the dust is optically active. Thin coatings of ≤3 μm particles covering less than 14 per cent of the sample surface demonstrated significant

Table 1. Summarizing the effects of environment, particle size, and albedo on features of TIR spectra as discussed in several studies. Spectral features of interest include the CF, RB, TF, and overall spectral contrast. ↑↓ symbols indicate increasing and decreasing respectively, while → indicates shifts to longer wavelengths and ← to shorter wavelengths. Yellow indicates correlations being explored in this study while green denotes consistent effects already observed in preliminary observations.

	Contrast	RB strength	RB min Emissivity	CF position	Emissivity shortward CF	TF strength
Pressure↓	↑(fines) ↓(chip)			←		
Albedo↓	↓		↑	→		
Particle Size ↓ *SAE*	↑	↑	↓	→	↓	↑
Particle Size ↓ *Ambient*	↓		↑			↑
Coating Thick. ↑ *Ambient*		↓			↓	
Dark *SAE* vs. Dark *Ambient*				←		↓

spectral effects distinct from those observed for thick layers. These results confirm the hypothesis that dust coatings can alter TIR spectra in non-systematic ways, highlighting the need to distinguish between optically thin and thick coatings. Previous work on factors affecting TIR spectroscopy are summarized in Table 1 (Logan et al. 1973; Salisbury & Walter 1989; Henderson et al. 1996; Donaldson Hanna et al. 2012, 2014, 2017, 2019; Pan et al. 2015; Thorpe et al. 2015; Hardgrove et al. 2016; Glotch et al. 2017, 2018; Schrader et al. 2017; Breitenfeld et al. 2019; Shirley & Glotch 2019).

3. REGULATED ENVIRONMENT CHAMBER FOR DEPOSITION OF THIN AND DISCONTINUOUS DUST COATINGS

Previous methods used to simulate dust deposition include sifting (Crisp & Bartholomew 1992), alcohol suspension (Singer & Roush 1983; Fischer & Pieters 1993), lofting via compressed air (Wells, Veverka & Thomas 1984; Johnson & Grundy 2001; Johnson et al. 2002; Rivera-Hernandez et al. 2015), and mechanical agitation/settling (Graff et al. 2001; Graff 2003). The dust deposition chamber built in this study uses elements from these methods to enable accurate and repeatable dust coatings up to 1000 μm thick. The chamber and its six subsystems are shown in Fig. 4. The enclosure (1) is designed to hold laboratory N_2 at 1 atm to reduce unwanted electrostatic effects that lead to excessive clumping. Dust is manually loaded into the agitation basket (2) where it is radially distributed by the agitator (3). The basket is surrounded by 2-mm holes that allow lofted dust to enter the chamber in an efficient manner without oversaturating the environment or grouping to one side. Dust is then further distributed through lofting by six low-velocity computer fans (4). The chamber operates in cycles utilizing 0.5 g of dust over a 150-s period. This cycle is repeated until negligible amounts of the dust are expunged from the basket and lofted in the enclosure. A maximum of 2 g can be loaded into the basket at one time and cycled until empty. Thinner coatings with low spatial density require less total input dust and fewer cycles, while thicker coatings with high density require significantly more cycles. For exceptionally thin coatings, a sieve can be installed over the sample to further control particle size and prevent deposition of clumped particles ejected early in the agitation phase. While spatial coverage and continuity are inherently tied, they can be

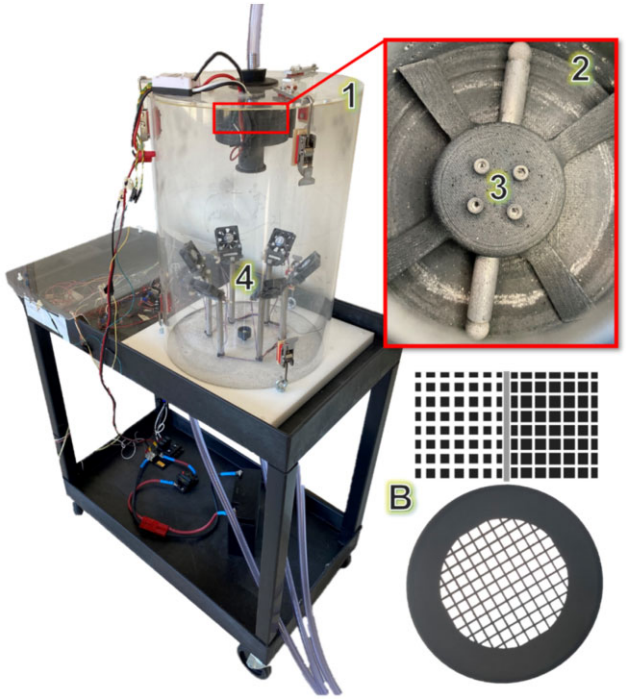

Figure 4. Dust deposition chamber designed and used for this study. Image outlined in red shows an internal view of the agitation basket. Subsystems are labelled by numbers: enclosure (1), agitation basket (2), agitator (3), and lofting fans (4). The chamber enclosure is 355 mm in diameter. (B) Top demonstrates two desired discontinuous patterns (25 and 50 per cent coverage) while bottom shows an example mask that is 30 mm in diameter and designed to fit over the spectrometer's sample cups.

individually studied through selective masking of substrate surfaces. Two different deposition masks (Fig. 4, B) are used to simulate discontinuous checkerboard patterns that cover ∼25 per cent and 50 per cent of the substrate surface. Deposition masks are three-dimensionally (3D) printed using the commercial material Accura® Xtreme™ White 200 through stereolithography to ensure a ≤50 μm minimum feature resolution and smooth surface finish. Speed and operation times for each stage of a deposition cycle are precisely managed according to 28 calibrated variables in a custom Arduino IDE program. An aluminium substrate is used to fill the sample holder and provide a smooth reference surface during calibration and repeatability testing. The agitation fan speed is adjusted so dust is distributed from the centre of the enclosure but not ejected into the walls of the chamber. The lofting fan speed was calibrated similarly, ensuring the dust is picked up by the flow of the fans but not ejected into the chamber edges. The agitation time of 60 s is set to ensure minimal dust is left inside the agitation basket after the end of each cycle. Agitation is bi-directional and non-symmetric to reduce clumping of stagnant sample in the basket. Lofting occurs for 90 s followed by 1 min of airfall.

4. MEASURING DUST COATING THICKNESS, COVERAGE, AND POROSITY

Physical parameters of the dust coating structure have strong effects on TIR spectra due to scattering (Salisbury & Wald 1992), changes in overall albedo (Breitenfeld et al. 2019), and increased obscuration (Johnson et al. 2002). Constraining the thickness, spatial coverage,

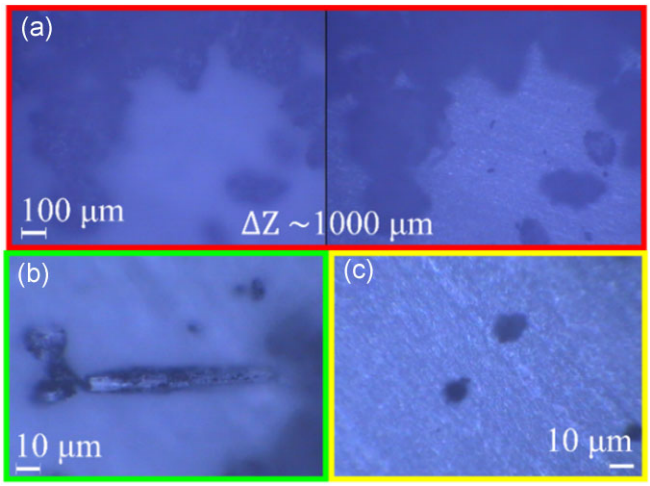

Figure 5. Microscope images of dust coated samples, with the substrate appearing as a light coloured solid background and the darker dust on top in patches or isolated particles. (a) Showing a macro-discontinuous dust coating roughly 1000 µm in thickness at the bottom (right panel) and top (left panel) *Z*-axis focal points. (b) Example of a 'stick' particle not counted in measurement due to its aspect ratio. (c) Typical 10-µm dust particle used for coatings in this study.

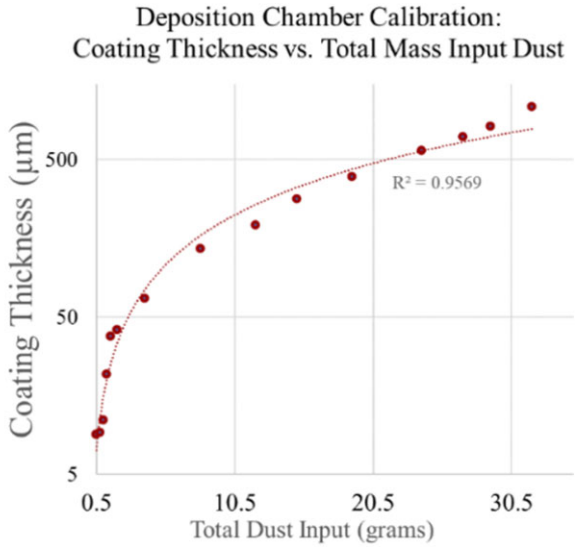

Figure 6. Calibration of the dust deposition chamber showing the total input dust required for coatings ranging from 10 to 1000 microns in thickness. Dotted line shows a power-law fit indicating increasing return on input mass invested.

and porosity of each sample is essential to determine the spectral and thermophysical effects that particular coating structures may cause.

Coating thickness is measured relative to the exposed substrate using a WITec confocal microscope with sub-micron focus precision. Dust coating thickness is estimated as an average of 50 measurements of the difference in Z stage positions for the focal point of the closest exposed substrate (Fig. 5a, right panel) and top of the dust layer (Fig. 5a, left panel). Particles with an aspect ratio greater than 2:1 are discounted from measurement (Fig. 5b), as their orientation may strongly bias measured coating thickness. The microscope optics is electrostatically discharged prior to measurement to prevent loss of tall samples during base measurements. Several coatings were created spanning thicknesses ranging from 10 to 1000 µm, with an increasing return on coating thickness per mass of dust invested. This is expected due to dust accumulating on edges and on surfaces of the chamber, which is continuously re-lofted, with the potential to airfall on to the sample. These measurements populate calibration curves that estimate the number of deposition cycles required to achieve a desired thickness (Fig. 6). Spatial coverage for MiD and macro-discontinuous coatings is measured optically through a pixel count of stitched microscope images using the GNU Image Manipulation Program. Slumping and erosion of dust columns after mask removal in especially thick macro-discontinuous samples can lead to an increase from the expected exposed surface upwards of 40 per cent. Coating porosity is constrained by weighing the sample and sample cup before and after deposition then calculating volume from the average coating thickness and assuming the density of antigorite (2.5 g cm^{-3}).

5. DUST, PARTICULATE, AND CHIP SAMPLE PREPARATION

For this work, both the substrate and dust are sourced from antigorite; the dominant analogue mineral used in mixtures simulating complex CI and CM analogue mixtures used to simulate Bennu's spectra (Howard et al. 2011; Breitenfeld et al. 2021, 2022). While it would be ideal to use a chondritic spectral analogue to Bennu, the amount of material required is prohibitive. Using an analogue material like antigorite may not result in OTES spectral matches, yet it does help constrain changes due to dust coatings in an SAE. 425 g of antigorite (Fig. 7A) sourced from Cedar Hill Quarry (Lancaster County, PA)

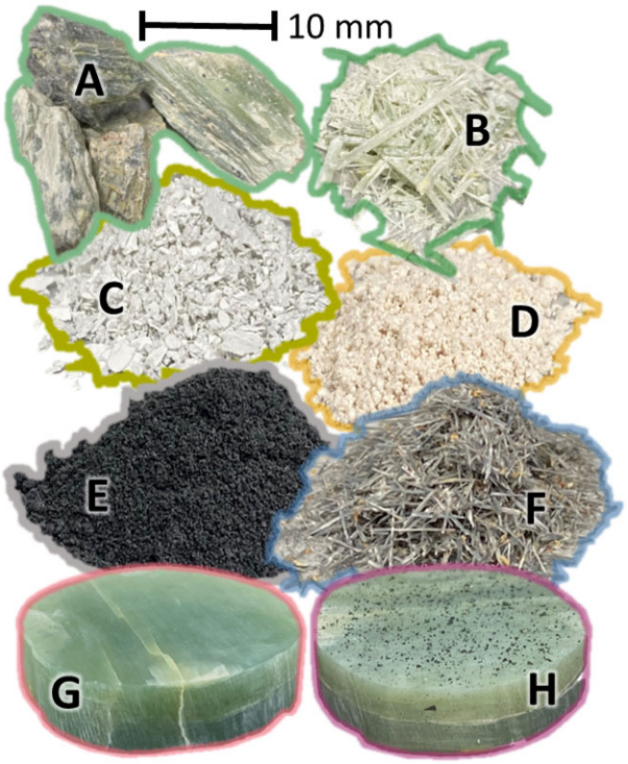

Figure 7. Showing multiple stages of the sample preparation process including the original antigorite sample (A–B), ≤10-µm dust (C), baked dust (D), baked darkened dust (E), 180- to 250-µm baked particulate (F), polished chip (G), and polished chip with an MiD (≤10 µm) visible coating (H).

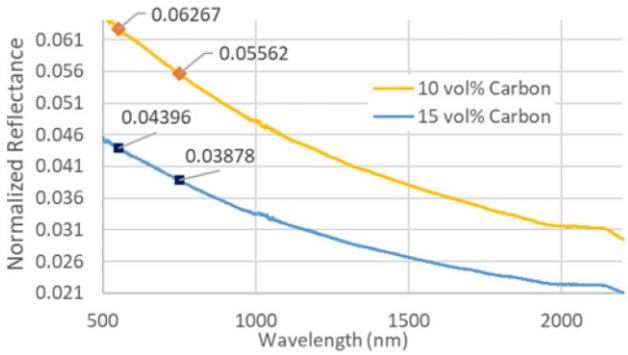

Figure 8. Reflectance spectra of antigorite dust darkened with 10 and 15 volume per cent carbon lamp black. The 15 volume per cent mixture was chosen to achieve a visible albedo like that of Bennu, indicated by the sample's reflectance labelled at 550 nm (0.044) and 750 nm (0.039).

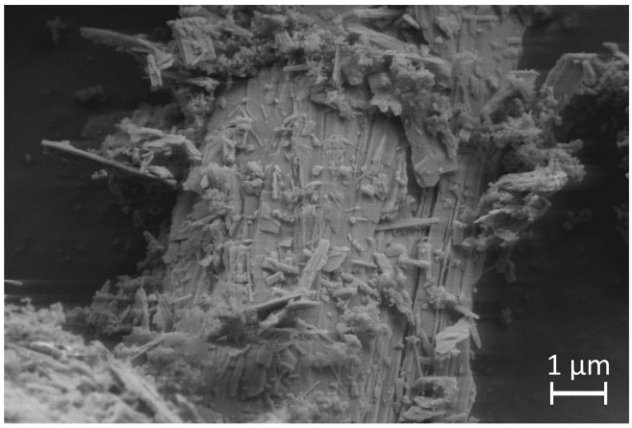

Figure 9. SEM image showing a grain of the baked and darkened antigorite dust (Fig. 7E) acquired using SE2 with 2.5 keV. While most of the particles are smaller than 10 μm, a small proportion of them are less than 100 μm along a single axis. Additional SEM images of the dust used in this study are available in the Supplemental Materials.

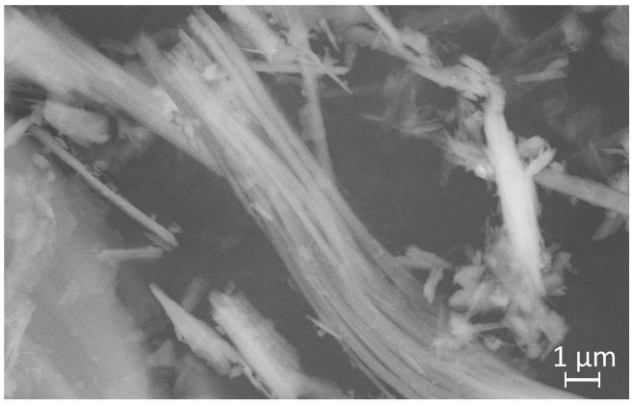

Figure 10. SEM image of the baked antigorite dust (Fig. 7D) acquired using an RBSD with 20 keV. This method makes thicker particles opaque and smaller objects transparent. The most prominent feature shown in this lower density region is thin, long, and highly fibrous. Additional SEM images of unbaked dust and baked darkened dust are available in the Supplemental Materials.

was purchased from Excalibur Mineral Corporation. To generate antigorite dust, the sample is hand-ground in a mortar and pestle to roughly 300 μm (Fig. 7B) before loading into a McCrone micronizing mill. After 15 min of wet grinding in ethanol, the ≤10-μm size fraction (Fig. 7C) is separated in ethanol using Stokes' settling method (Day 1965) and confirmed using a Malvern Mastersizer 2000 laser diffractometer, as demonstrated by Sperazza, Moore & Hendrix (2004). The ≤10-μm size fraction dust is then baked at 500°C for 24 h to remove hydration features (Fig. 7D) according to the methods described in Che et al. (2011) and Che & Glotch (2012). While Bennu has 2.7-μm features suggesting the presence of OH, it does not have a strong 3-μm feature indicative of H_2O (Hamilton et al. 2019). Based on Breitenfeld et al. (2021), nanophase carbon lamp black is mixed with the dust (Fig. 7E) to achieve a visible albedo consistent with Bennu (∼0.04, Clark et al. 2011; Breitenfeld et al. 2019). The amount of nanophase carbon lamp black added was adjusted according to preliminary measurements of the mixture's albedo using an ASD FieldSpec 3 Max spectrophotometer to measure the reflectance at 550 and 750 nm referenced to a calibrated Spectralon® standard. Visible and near-infrared spectra of two reference mixtures including 10 and 15 volume per cent carbon are shown in Fig. 8. Coarse particulate substrates (180–250 μm) were created by wet and dry sieving hand-ground antigorite then washing with ethanol to remove clinging fines (Fig. 7F). Coarse particulates were also baked at 500°C for 24 h to remove hydration features as described above. Chip substrates were cut, sanded, and polished in water to fit the sample cup and provide a smooth reference surface (Fig. 7G). Immediately after shaping, the chips were dried at a low temperature (<150°C) for 3 h. Nanophase carbon is only added to the dust, as it does not stick to the chip or particulate substrate. Fig. 7H depicts what chip substrates (Fig. 7G) look like when coated with baked darkened dust (Fig. 7E). Dust particles produced by this method were characterized using scanning electron microscopy (SEM) and energy dispersive spectroscopy to further constrain their morphology and chemistry. Fig. 9 shows an SEM image of the baked darkened antigorite dust (Fig. 7E), acquired with a 2.5-keV accelerating voltage and a secondary electron detector (SE2). Fig. 10, acquired with 20-keV accelerating voltage and a Robinson Backscatter detector (RBSD), shows a single fibrous grain of baked dust (Fig. 7D) with streaks of gaps or very thin material along its splinter axis. These images highlight the fibrous nature of antigorite, as the mineral splinters at each stage of processing and still retains its needle-like morphology at the sub-micron scale. This makes the control of particle size during sample preparation and dust deposition uniquely challenging. Mechanical sorting methods, such as sieving, and most density-based methods cannot account for extreme dimensional ratios. The morphology of this material has a strong impact on the way thermal energy is exchanged between particles, especially in an airless body environment. The process by which this dust is deposited has a strong impact on the overall coating porosity as elongated particles have the potential to be in either full (parallel) contact with each other, partial contact at an angle, or perpendicular to one another with minimal intersection. This leads to variations in physical properties among twin samples produced using the same procedure, while also giving greater influence to the specific deposition process being used. Given these considerations, it becomes imperative to investigate different deposition methods in a laboratory setting to comprehensively characterize the coated samples that result from each. Specifically, analysing the airfall technique in comparison with conventional methods, such as sieving or pouring, helps isolate and understand the unique spectral and thermophysical properties dust coatings can have when forming on small, airless bodies. RT in these samples is expected to deviate from

models with the typical assumption of spherical or nearly spherical particles. This motivates future work that constricts particles to a single size in all axes and compares multiple ranges for their discrete impact on an observed spectrum.

6. PLANETARY AND ASTEROID REGOLITH SPECTROSCOPY ENVIRONMENTAL CHAMBER

TIR (5–50 μm) spectra of each sample are acquired under SAE conditions using the Planetary and Asteroid Regolith Spectroscopy Environmental Chamber (PARSEC) at Stony Brook University (Shirley & Glotch 2019). PARSEC was modelled after the chamber described in Thomas et al. (2012) to measure samples under environmental conditions typical of airless bodies. The chamber houses a sample wheel with six sample cups and a blackbody calibration target coated with Nextel black. There is an additional blackbody target under the wheel. All sample cup and blackbody targets can be individually heated and rotated into position from outside of the chamber. Temperature is controlled through two Eurotherm® Mini8® loop controllers and managed on an in-lab computer with the Eurotherm iTools interface. Samples are illuminated at 55° incidence by a quartz halogen lamp connected to a Bentham 610 power source. Surrounding the sample wheel is a cold shield actively cooled by the input of liquid nitrogen into an internal dewar to reach temperatures less than −125°C. Pressure in the chamber is controlled by a Pfeiffer HiCube turbo vacuum pump to reach 10^{-6} mbar. In line with the vacuum chamber is a pressure regulated tank of N_2 used for purging and ambient pressure measurements. The PARSEC chamber is connected to a Nicolet™ 6700 Fourier-transform infrared spectrometer equipped with a Caesium Iodide (CsI) beamsplitter and a deuterated L-alanine doped triglycine sulfate detector with a CsI window. The spectrometer is actively purged with air scrubbed of CO_2 and water vapour and sealed at the interface with PARSEC. A total of 256 scans from 4000 to 225 cm^{-1} are integrated for a 10-min measurement period, using a spectral sampling of 2 cm^{-1}.

During each experimental session, three samples and the blackbody are measured under SAE conditions. Calibration measurements of the blackbody target at 70 and 100°C are acquired, then the integrated sample cup heaters and solar lamp are adjusted to achieve the desired sample brightness temperature of 80°C. Samples are allowed to reach temperature under the lamp for more than 45 min until the spectral maximum stabilizes and the calculated brightness temperature at the CF is within ∼10°C of the target 80°C. This procedure is repeated for all three samples while ensuring the chamber temperature remains stable under −125°C through continued addition of liquid nitrogen. Following SAE measurements, the chamber is allowed to warm up overnight while under vacuum. Once at ambient temperature (∼25°C), the chamber is incrementally filled with nitrogen as slow as mechanically capable to ensure minimal effects on delicate dust coatings. The coating thickness, coverage, and porosity are measured before and after each set of spectra are acquired to characterize layer disturbances during pumping operations, if they occur.

Two kinds of radiance-to-emissivity conversions can be used with PARSEC data (Breitenfeld et al. 2021). A laboratory method used by Ruff et al. (1997) assumes emissivity at a single brightness temperature, while a second method developed for use with OTES data (Hamilton et al. 2019; Breitenfeld et al. 2021) accounts for variable temperatures in the field of view. The Ruff et al. (1997) method determines the maximum brightness temperature between 500 and 1700 cm^{-1} and divides the radiance by a Planck function of the same temperature. This assures the maximum brightness temperature is the kinetic temperature of the same, and its emissivity is unity at the frequency of this maximum (Realmuto 1990). The OTES method simulates OTES L3 'mt_emissivity' processing by replacing a single Planck function with a linear least squares model derived from a range of temperatures (Breitenfeld et al. 2021). Each spectrum is fit to a range of Planck functions associated with different temperatures in a linear least squares model. The measured radiance is divided by the modelled radiance divided by.97 (Hamilton et al. 2019). Excluding high noise data in lower wavenumbers, the spectra are normalized, and sampling is reduced using a cubic spline interpolation to ∼8.66 cm^{-1} per channel, matching that of OTES. All data presented in this study have been converted using the laboratory method, while the OTES method accounting for variable temperatures will be used in future work in order to better align with 3D thermal models of these dust coating scenarios.

Table 2. Experimental parameters driving coatings created in this study. These parameters describe a range of values that shift according to batch results in order to accurately capture spectral trends and their source. Parameter values start at a baseline with a wide variance in the preliminary investigation and will not be entirely defined until completion of the full 72-permutation study. Once defined, parameters will describe a range of values for that coating property which result in similar spectral and thermophysical effects with minimal variability. A table showing all 72 permutations of these parameters is provided in the Supplemental Materials.

Substrate	Continuity	Thickness	Micro-discontinuous masking	Macro-discontinuous masking
Chip	Micro	Thin	Visible	Ring mask
Particulate	Macro	Half	Opaque	20% masked
			Dense	50% masked
	Continuous	Max	Continuous	

7. ANALYTICAL METHODS

As discussed in Section 2, several environmental and sample variables have strong effects on TIR spectra. Due to the method of deposition in this study, some sample variables are inherently interconnected, and only vary independently because of mechanical error. For example, increasing coating coverage decreases overall albedo due to the dust being darker than the substrate. Increasing coating thickness leads to an increase in coverage up until the first dust layer entirely masks the substrate. Trends found between coating structures and spectral features need to be unbound from variance in coverage (albedo), coating thickness, and porosity to be useful in orbital analyses where few properties are constrained. Deconvolving the individual effect a variable has on the resulting spectra requires a systematic exploration of its entire range, both including and excluding other variable extremes.

The structure of each sample coating is constrained by five experimental variables and the terminology used to describe their scales (Table 2). In total, these groups introduce 72 different permutations of sample properties. The specific minimum and maximum values which define these parameters will be determined based on where significant spectral trends occur after the full 72 sample study is complete. Parameters such as the substrate and continuity have static, qualitative definitions which do not have uncontrolled variance between samples. On the other hand, sample parameters such as thickness and coverage are dynamic quantitative definitions that are used to target a particular range of values. These definitions accommodate an iterative experimental set-up that systematically

reveals spectral trends without relying on chance alignment with pre-selected experimental parameter values. In the preliminary investigation, controls and extremes for each parameter are selected to establish a baseline understanding of the spectra and help identify trends between two samples with wide variance in a single parameter. Extremes are selected based on limitations of the deposition method and PARSEC. For example, coating thickness can be characterized through early analysis of a polished chip (control), 10 μm coated chip (extreme minimum), and 1000 μm coated chip (extreme maximum), providing spectra that host features at the top and bottom bounds of the influenced spectral trend. Batches that follow from this are adjusted to target between these bounds and iterate until the region of transition from one state of the spectral feature to another has been revealed. The definition of the 'max' thickness parameter, e.g. may therefore change as the range of values is narrowed, and the specific thickness at which its effects are present in spectra becomes known. This method creates definitions which are not dependent on restrictions specific to the experimental set-up, and instead, constrains the range of sample property values based on their distinct effects on spectra.

To avoid missing the introduction or progression of a spectral trend, the degree to which each parameter value is changed will depend on previous iterations' responses. Instead of incrementing a single parameter a small amount across an extensive range, which would be resource-intensive, these experimental parameters are adjusted in iterative batches to optimize the use of raw materials and align with the operation cycle of PARSEC. This approach facilitates meticulous tracking of spectral feature changes across specific parameter ranges, ensuring precision in identifying critical transition points within these trends. The importance of this method lies in the necessity to uncover not only the occurrence of each spectral trend but also its underlying factors and mechanisms.

Calculated parameters such as porosity are excluded from determining sample selection, as creating target porosities would require too many samples across a wide variance. Because this work depends on a mineralogical analogue, the acquired spectra will not be directly relatable to orbital observations of Bennu. Antigorite exhibits significantly higher spectral contrast and lacks several minor features attributable to mineralogical variability in the Bennu OTES spectra. Additional spectral features, such as those introduced by carbon lamp black and remnant air/water in the spectrometer housing, must be either accounted for in analyses or ignored when comparing with orbital results. Mineralogical analogues and spectral indices are best used as a guide to identify extremes and trends in data, rather than as a cross-reference for specific spectral features (Breitenfeld et al. 2021; Hamilton et al. 2021). Spectra from this study are compartmentalized and parametrized using spectral indices and individual feature morphology. These analytical parameters are incorporated into quantitative and qualitative comparisons with the properties of dust coatings to determine their potential origin. Some example quantitative parameters may include the position or strength (depth) of key features, such as the CF and RB. Spectral indices are chosen to best highlight features that change across coating types. Qualitative parameters, such as the type of coating continuity, are also considered in these analyses. A principal component analysis (PCA) is conducted on both emission spectra and the listed quantitative parameters. PCAs have been used before to discern spectral trends and features and effectively elucidate bands and absorptions, which are important to the target trend (Xie et al. 2022). A multiple correspondence analysis is used concurrently to discern relationships between qualitative sample properties, and group potentially related spectral trends found by the PCA. Combining these analytical techniques simplifies spectral data into fewer dimensions and intelligible patterns while reducing contextual specificity of the proposed trends.

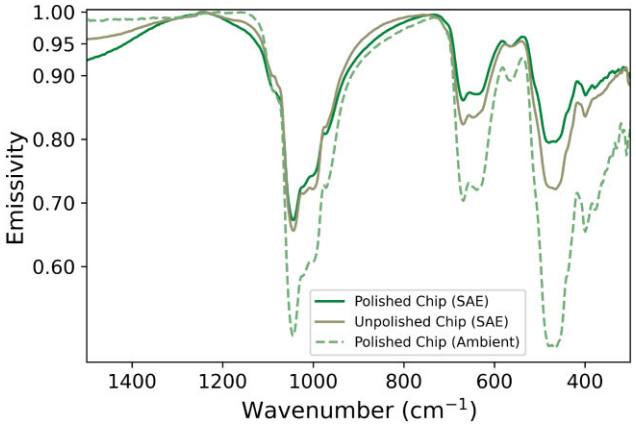

Figure 11. SAE spectra of an unpolished and polished antigorite chip, along with ambient spectra of the polished chip.

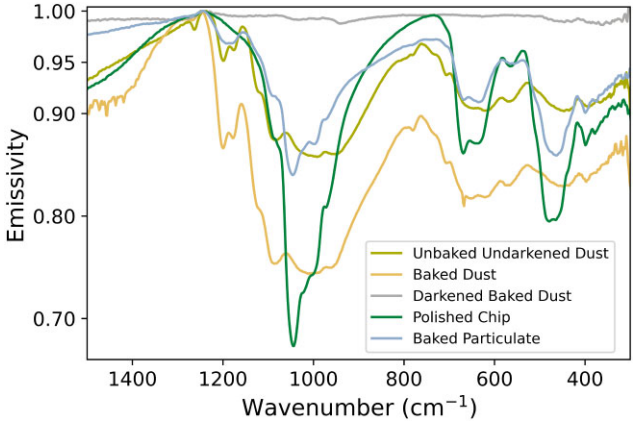

Figure 12. SAE spectra of several control samples including dust at each stage of the sample preparation process.

8. PRELIMINARY AND CONTROL RESULTS

Several SAE and ambient spectra were acquired for a variety of experimental extremes to establish baseline and threshold capabilities of the dust deposition chamber. Controls were established by taking spectra of each material at each stage of the sample preparation. Polished chips (dark green, Fig. 11) exhibited slightly lower spectral contrast at longer wavelengths than unpolished chips (dark yellow, Fig. 11). The CF of the unpolished chip is shifted to slightly longer wavelengths, likely a result of smaller particle size surface features that would have been smoothed out and removed through the polishing process. Consistent with the previous studies outlined in Section 2, the polished chip acquired under ambient conditions (dashed dark green, Fig. 11) exhibits increased spectral contrast and a CF shifted to longer wavelengths compared with that acquired under SAE conditions. Consistent with previous studies under SAE conditions (Glotch et al. 2018), the polished chip (dark green, Fig. 12) exhibited the highest contrast while the baked particulate (light blue, Fig. 12) had the lowest of any undarkened sample. As expected from reductions in albedo, baked dust (yellow, Fig. 12) has the highest contrast compared with darkened baked dust (grey, Fig. 12). Consistent with previous work investigating the effects of

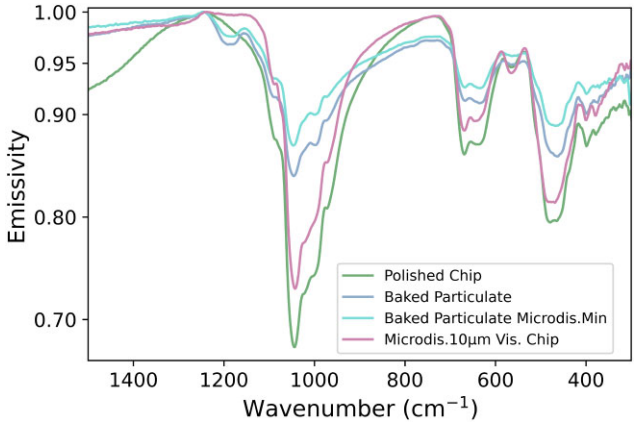

Figure 13. SAE spectra of the chip and baked particulate substrates alongside their counterparts with the smallest visible MiD coatings of darkened baked dust possible (≤10-μm thick).

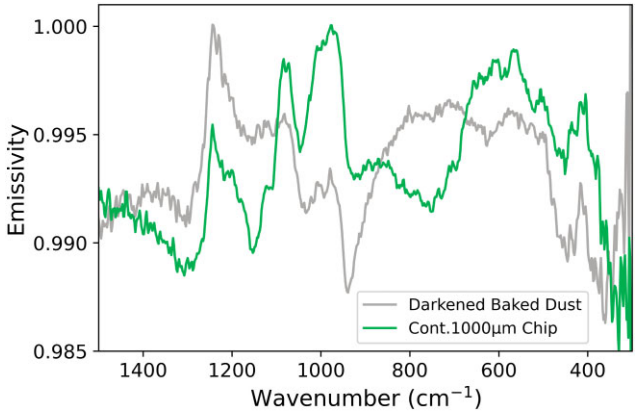

Figure 14. Comparing the SAE spectra of darkened baked dust with a chip continuously coated with 1 mm of the same dust.

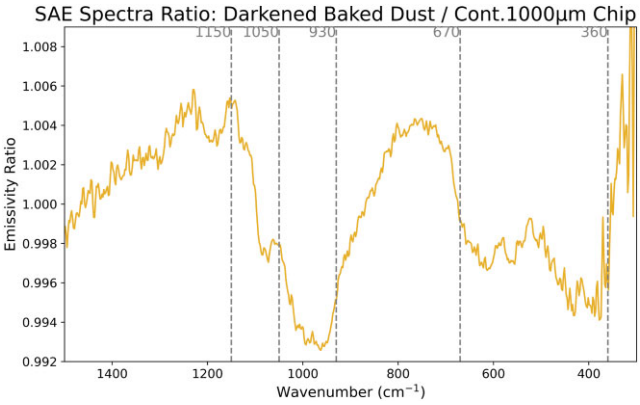

Figure 15. Spectral ratio between darkened baked dust and the polished chip coated with the maximum of 1 mm of continuous dust. Highlights differences between these spectra which may be a result of porosity variability from deposition of dust and/or direct effects from the underlying substrate. Locations of interest are labelled as grey vertical dashed lines.

baking on serpentine group minerals (Che & Glotch 2012), unbaked undarkened dust (dark yellow, Fig. 12) has a lower spectral contrast compared with baked dust. The broad absorption feature centred around ∼1050 cm^{-1} is wider and deeper in the baked dust spectrum than in its unbaked undarkened counterpart. The CFs of all spectra featured in Fig. 12 are within 5 cm^{-1} of each other. Samples of dust, encompassing all particle sizes less than 100 μm, exhibited multiple local minima associated with double absorption features centred around ∼1190 cm^{-1}. The baked particulate also showed a single local minimum at this wavelength.

The addition of a 10-μm-thick MiD coating to a polished chip sample (purple, Fig. 13) resulted in a slightly lower overall contrast, and increased emissivity longward of the CF (Fig. 13). The silicate emissivity roll-off at wavelengths shortward of the CF is significantly reduced for the coated chip. A micro-discontinuously coated particulate sample (cyan, Fig. 13) was made with the minimum amount of dust that can be deposited in one cycle, resulting in a nearly negligible coating. The coated baked particulate exhibited only a slight reduction in spectral contrast when compared with the uncoated baked particulate (light blue, Fig. 13). The local minima present at ∼1190 cm^{-1} in both baked particulate spectra are barely visible in the 10-μm-thick micro-discontinuously coated chip and not present for the polished chip (dark green, Fig. 13) alone. Two optically thick samples were prepared to assess the maximum coating height achievable within the constraints of the sample preparation and analysis procedure. The polished chip continuously coated with the maximum 1 mm of dust (green, Fig. 14) exhibited some similar spectral features to the darkened baked dust alone (grey, Fig. 14) but had significant differences in slope and shape occurring between ∼1150 and 670 cm^{-1} (Fig. 14). Fig. 15 illustrates differences between these spectra through a spectral ratio. An emissivity minimum present in the darkened baked dust (grey, Fig. 14) at 360 cm^{-1} is shifted to 330 cm^{-1} in the chip coated with 1 mm of continuous dust. Between 1150 and 1080 cm^{-1}, the coated chip exhibits a pronounced upward slope towards an emissivity peak at 1080 cm^{-1}, while the darkened baked dust maintains a slightly positive slope before gradually declining after 1080 cm^{-1}, matching the coated chip's slope towards 1050 cm^{-1}. While sharing absorption features at ∼1150, ∼1050, and ∼930 cm^{-1}, the width of each feature is significantly greater in the darkened baked dust alone. Additionally, following each emissivity minimum (shortward), there is always a strong difference in slope between the 1-mm coated chip and darkened baked dust. Overall, the magnitude of these differences is significant given that all components of the coated sample are of the same source material, and emission from the substrate is not expected to cause drastic effects as far as 1 mm through continuous dust. The substrate likely plays a pivotal role in facilitating heat transfer from the sample cup heaters below, just as the thick coating of dust affects heat transfer from the solar lamp above. This underscores the crucial importance of constraining coating porosity, thickness, and continuity when characterizing the spectral and thermophysical properties of dust coated boulders. It is possible that differences between these spectra are a direct result of the deposition method used when loading dust into the PARSEC sample cups manually compared with when depositing them using the chamber. This outcome instils confidence in the custom deposition chamber nitrogen airfall technique as a feasible representation of dust deposition and coating formation on a small, airless body. However, it also highlights the necessity for a future sample to be created where a cup is filled ≥50 per cent with dust deposited by the chamber. More samples with closer matching porosities will be required to determine if these differences are induced by substrate emission or differences in the dust structure.

A polished chip was coated with a 300-μm-thick macro-discontinuous pattern covering 60 per cent of the surface (dark blue, Fig. 16). The spectra of this sample exhibited the same overall

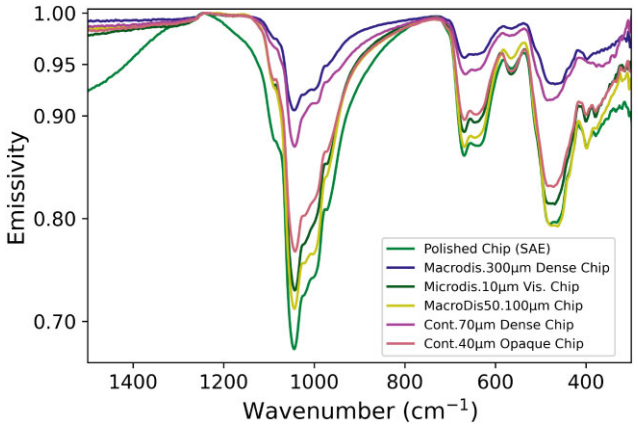

Figure 16. SAE spectra of the polished antigorite chip compared with several coatings with varying continuity, thickness, and coverage.

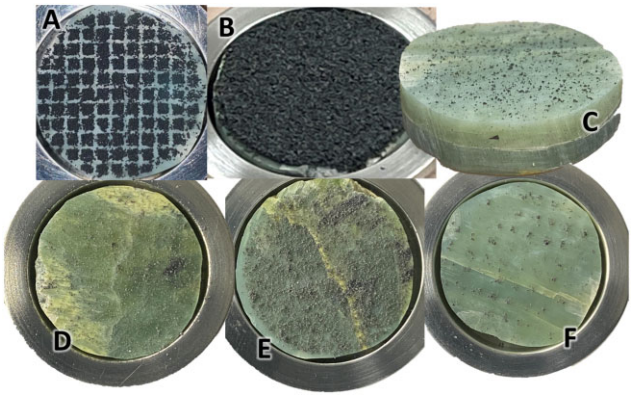

Figure 17. Example dust coatings and their thickness: (A) macro-discontinuous (300 µm), (B) continuous (1 mm), (C) MiD (≤10 µm) visible, (D) continuous (40 µm) opaque, (E) continuous (70 µm) dense, and (F) macro-discontinuous visible.

shape as the chip alone (light green, Fig. 16), but at a much lower contrast. Like that for the MiD coatings (dark green, Fig. 16), the silicate emissivity roll-off at wavelengths shortward of the CF is significantly reduced and the emissivity longward of the CF is much higher compared with the chip alone. The continuously coated 40-µm-thick coated chip (light red, Fig. 16) and its 70-µm-thick counterpart (purple, Fig. 16) showed very similar spectral shapes with the thinner coating having a much higher contrast. The 300-µm-thick macro-discontinuous coated chip (dark blue, Fig. 16) featured a very similar shape and only slightly lower contrast compared with the continuously coated 70-µm thick chip. The 100-µm-thick macro-discontinuous pattern covering 50 per cent of the chip surface (yellow, Fig. 16) has a slightly higher contrast compared with the continuously coated 40-µm-thick chip (light red, Fig. 16) and 10-µm-thick MiD coated chip (dark green, Fig. 16). These similarities suggest the significance of even some (≤50 per cent) substrate exposure when it comes to the TIR spectral effects of both thin and thick coatings. Images of example dust coatings used for these preliminary results can be found in Fig. 17.

These preliminary results demonstrate which experimental variables spectra are sensitive to while providing boundary conditions for the systematic analysis of all potential trends. These results encourage more fine iterations of coating properties for optically thin coating samples, while demonstrating a reduced need for variety

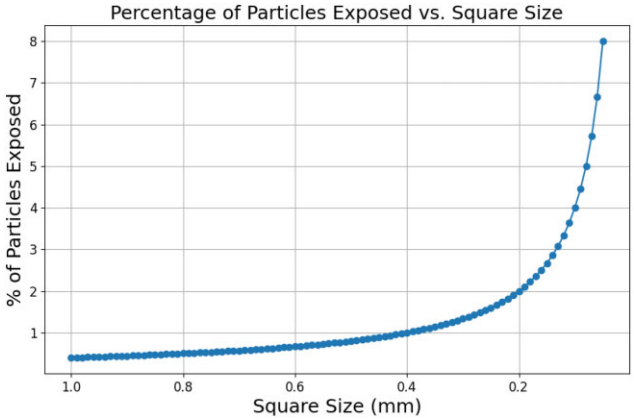

Figure 18. A simple 2D mathematical model showing the percentage of dust particles exposed to environment at the perimeter of squares in a grid pattern of decreasing unit size and constant coverage. This model assumes 1 micron diameter dust particles coat a 10-mm-radius sample with 50 per cent coverage. The size of the squares in the macro-discontinuous pattern is plotted from 1 to 0.05 mm and their distance is adjusted to maintain constant area of coverage. As square size decreases, the percentage of particles exposed on the edges of squares exhibits hyperbolic growth towards a maximum of 8 per cent for the minimum square size of 0.05 mm.

in coating thickness for samples greater than ∼200 microns. These results also provide early confidence that coating patterns and their continuity have an effect on TIR spectroscopy and thermal modelling. Macro-discontinuous patterns used in this preliminary investigation are low density (large groups of particles) and expose a greater proportion of grains to contact with other dust particles compared with high-density, smaller grid patterns, especially when considering the spot size of PARSEC (∼1 cm). This means that the degree of contact particles make with the vacuum environment on average for any given sample is related to the percentage of coverage and the unit size of each square in the pattern. This is shown in Fig. 18, which models the percentage of total particles exposed to environment in 2D space as the square size of a macro-discontinuous pattern decreases. This effect is reminiscent of the coastline paradox, where the length of a coastline appears to be infinite if measured with an instrument of infinitesimal size. This suggests that the continuity and pattern scale of dust coatings have a direct influence on the exchange of thermal energy between dust, substrate, and the vacuum environment. More samples with higher density macro-discontinuous patterns (smaller groups of particles) will be required to determine if the associated spectral trends are consistent above and below the effective resolution of the sensor in question.

9. FUTURE WORK

The primary objective of this phase in the study was to comprehensively characterize the laboratory and analytical methods essential for examining the TIR spectroscopic effects of dust coatings on airless bodies. This preliminary phase provides a platform for identifying experimental variables and spectral trends of interest while ensuring the technical robustness of the methods. This manuscript discusses the study's motivation, outlines the development and manufacturing of the experimental set-up, and demonstrates the systematic examination of nuanced and interconnected spectral effects at a smaller, preliminary scale. This approach allows for fine-tuning of methods, including sample characterization, dust deposition, sample measurement, and spectral feature analysis. Importantly, these preliminary

phase results are crucial to planning a set of sample permutations that reveal significant spectral trends within an applicable range of coating and substrate properties. The commitment to exhaustively analyse all 72 permutations is a fundamental element of the study's design. The insights gleaned from this preliminary subset of samples offer focused guidance in determining the most relevant coating variables and their intricate relationships with spectral features and trends. These findings reduce the scope of coating variations necessary to fully characterize spectral trends that are important to the study. This methodological refinement guarantees that our ultimate comprehensive analysis will efficiently yield robust insights into the underlying mechanisms governing the spectral and thermal characteristics of dust-coated surfaces on airless bodies.

Following the acquisition of all 72 experimental permutations and analysis of their spectral trends, a series of thermal simulations will be used to replicate the conditions of the dust coating samples in PARSEC. RT-based thermal models similar to those implemented by Hale & Hapke (2002) and Millán, Thomas & Bowles (2011) are in development to provide a better understanding of vertical and lateral temperature distributions within dust layers and how they relate to the measured TIR emission spectra. By comparing the thermal model results with spectroscopic results, we will determine whether there is a dust coating scenario that can explain both the spectroscopic and thermophysical properties of low thermal inertia boulders on Bennu. As discussed in Section 5, the antigorite dust used in this study does not consist of nearly spherical particles which would align best with the assumptions used to drastically simplify thermal models. To address this, future work could include paired studies that explore the thermophysical and spectral effects of coatings using non-analogous materials with near-spherical particles, as well as utilizing near-analogue materials with asymmetrical particles. These concurrent investigations can collectively shed light on the interplay between particle geometry and other critical physical properties of the coatings, while specifically isolating spectral effects associated with particle asymmetry. Such an approach bolsters confidence in trends related to other experimental parameters, providing results relevant to laboratory, model, and real-world conditions. While this paired study falls out of scope for this work, there is substantial heritage for investigations that control particle size and geometry while characterizing spectral and thermophysical effects for the context of Mars and the Moon (Wechsler & Glaser 1965; Presley & Christensen 1997, 2010; Presley & Craddock 2006; Legrand et al. 2014; Ahern et al. 2021; Mellon, McKay & Grant 2022). Adapting these results or applying their methods to the context of airless bodies and CC materials would address gaps stemming from disparities between thermal models assuming spherical particles and laboratory spectroscopic results.

The deposition chamber designed for this study addresses a gap in laboratory analysis techniques by providing control over dust coating thickness and continuity. The methods introduced provide a robust platform for analysis of trends for coating porosity and particle structure. Development, calibration, and testing of the chamber have established the groundwork necessary to create direct comparisons of spectral and thermophysical properties related to dust coatings in airless body environments.

DATA AVAILABILITY

SEM images of all dust varieties are available in the Supplemental Materials. Spectra for each sample discussed in this study are available in Excel format on Zenodo (doi.org/10.5281/zenodo.7588266).

REFERENCES

Ahern A. A., Rogers A. D., Macke R. J., Thomson B. J., Kronyak R., Peters G., Carey E., 2021, LPI Contrib., 2548, 2290
Aronson J. R., Emslie A. G., 1973, Appl. Opt., 12, 2573
Biele J. et al., 2019, Prog. Earth Planet. Sci., 6, 48
Breitenfeld L. B. et al., 2019, LPI Contrib., 2132, 1866
Breitenfeld L. B. et al., 2021, J. Geophys. Res.: Planets, 126, 1
Breitenfeld L. B., Rogers A. D., Glotch T. D., Kaplan H. H., Hamilton V. E., Christensen P. R., 2022, Geophys. Res. Lett., 49, e2022GL100815
Che C., Glotch T. D., 2012, Icarus, 218, 585
Che C., Glotch T. D., Bish D. L., Michalski J. R., Xu W., 2011, J. Geophys. Res. E: Planets, 116, 1
Clark B. E. et al., 2011, Icarus, 216, 462
Crisp J., Bartholomew M. J., 1992, J. Geophys. Res.: Planets, 97, 14691
Day P. R., 1965, in Black C. A., Evans D. D., Ensminger L. E., White J. L., Clark F. E., eds, Methods of Soil Analysis, Part 1: Physical and Mineralogical Properties, Including Statistics of Measurement and Sampling. Am. Soc. Agronomy, Madison, p. 545
DellaGiustina D. N. et al., 2019, Nature Astron., 3, 341
DellaGiustina D. N. et al., 2020, Science, 370, 674
Donaldson Hanna K. L., Wyatt M. B., Thomas I. R., Bowles N. E., Greenhagen B. T., Maturilli A., Helbert J., Paige D. A., 2012, J. Geophys. Res.: Planets, 117, E00H05
Donaldson Hanna K. L., Cheek L. C., Pieters C. M., Mustard J. F., Greenhagen B. T., Thomas I. R., Bowles N. E., 2014, J. Geophys. Res.: Planets, 119, 1516
Donaldson Hanna K. L. et al., 2017, LPSC XLVIII, 1723
Donaldson Hanna K. L. et al., 2019, Icarus, 319, 701
Emery J. P. et al., 2014, Icarus, 234, 17
Fischer E. M., Pieters C. M., 1993, Icarus, 102, 185
Glotch T. D., Shirley K. A., Greenhagen B. T., 2017, LPSC XLVII, 1688
Glotch T. D., Edwards C. S., Yesiltas M., Shirley K. A., McDougall D. S., Kling A. M., Bandfield J. L., Herd C. D., 2018, J. Geophys. Res.: Planets, 123, 2467
Graff T., 2003, Master's Thesis, ASU
Graff T., Morris R., Christensen P., 2001, Lunar and Planetary Science Conference XXXII, 1899
Gundlach B., Blum J., 2013, Icarus, 223, 479
Hale A., Hapke B., 2002, Icarus, 156, 318
Hamilton V. E. et al., 2019, Nature Astron., 3, 332
Hamilton V. E. et al., 2021, A&A, 650, A120
Hardgrove C. J., Rogers A. D., Glotch T. D., Arnold J. A., 2016, J. Geophys. Res.: Planets, 121, 542
Henderson B. G., Lucey P. G., Jakosky B. M., 1996, J. Geophys. Res.: Planets, 101, 14969
Howard K. T., Benedix G. K., Bland P. A., Cressey G., 2011, Geochim. Cosmochim. Acta, 75, 2735
Johnson J. R., Grundy W. M., 2001, Geophys. Res. Lett., 28, 2101
Johnson J. R., Christensen P. R., Lucey P. G., 2002, J. Geophys. Res. E: Planets, 107, 5035
Lauretta D. S. et al., 2019, Nature, 568, 55
Legrand M., Dubovik O., Lapyonok T., Derimian Y., 2014, J. Quant. Spectrosc. Radiat. Transfer, 149, 219
Logan L. M., Hunt G. R., 1970, J. Geophys. Res., 75, 6539
Logan L. M., Hunt G. R., Salisbury J. W., Balsamo S. R., 1973, J. Geophys. Res., 78, 4983
MacLennan E. M., Emery J. P., 2022, Planet. Sci. J., 3, 47
Mellon M. T., McKay C. P., Grant J. A., 2022, Icarus, 387, 115211
Millán L., Thomas I., Bowles N., 2011, J. Geophys. Res.: Planets, 116, E12003
Moersch J. E., Christensen P. R., 1995, J. Geophys. Res.: Planets, 100, 7465
Mustard J. F., Hays J. E., 1997, Icarus, 125, 145
Nash D. B., Salisbury J. W., Conel J. E., Lucey P. G., Christensen P. R., 1993, J. Geophys. Res.: Planets, 98, 23535
Pan C., Rogers A. D., Thorpe M. T., 2015, J. Geophys. Res.: Planets, 120, 1984
Presley M. A., Christensen P. R., 1997, J. Geophys. Res.: Planets, 102, 9221

Presley M. A., Christensen P. R., 2010, J. Geophys. Res.: Planets, 115, E07003
Presley M. A., Craddock R. A., 2006, J. Geophys. Res.: Planets, 111, E09013
Ramsey M. S., Christensen P. R., 1998, J. Geophys. Res.: Solid Earth, 103, 577
Realmuto V., 1990, in Abbott E. A., ed., Proc. 2nd TIMS Workshop. Jet Propulsion Lab., Pasadena, p. 31
Rivera-Hernandez F., Bandfield J. L., Ruff S. W., Wolff M. J., 2015, Icarus, 262, 173
Rozitis B. et al., 2019, LPI Contrib., 2189, 2055
Rozitis B. et al., 2020, Sci. Adv., 6, eabc3699
Ruff S. W., Christensen P. R., Barbera P. W., Anderson D. L., 1997, J. Geophys. Res.: Solid Earth, 102, 14899
Salisbury J. W., Eastes J. W., 1985, Icarus, 64, 586
Salisbury J. W., Wald A., 1992, Icarus, 96, 121
Salisbury J. W., Walter L. S., 1989, J. Geophys. Res.: Solid Earth, 94, 9192
Salisbury J. W., D'Aria D. M., Jarosewich E., 1991, Icarus, 92, 280
Schrader D. L. et al., 2017, Lunar and Planetary Science XLVIII, 1273
Shirley K. A., Glotch T. D., 2019, J. Geophys. Res.: Planets, 124, 970
Singer R. B., Roush T. L., 1983, Lunar and Planetary Science Conference, 1358, 708
Sperazza M., Moore J. N., Hendrix M. S., 2004, J. Sediment. Res., 74, 736
Thomas I. R., Greenhagen B. T., Bowles N. E., Donaldson Hanna K. L., Temple J., Calcutt S. B., 2012, Rev. Sci. Instrum., 83, 124502
Thorpe M. T., Rogers A. D., Bristow T. F., Pan C., 2015, J. Geophys. Res.: Planets, 120, 1956
Wechsler A. E., Glaser P. E., 1965, Icarus, 4, 335
Wells E. N., Veverka J., Thomas P., 1984, Icarus, 58, 331
Xie B., Mao W., Peng B., Zhou S., Wu L., 2022, Minerals, 12, 508

SUPPORTING INFORMATION

Supplementary data are available at *RASTAI* online.

Supplemental Figures. SEM images of all dust varieties using SE2 (2.5 keV) and RBSD (20 keV).
Supplemental Table. Samples involved in current and future work including every permutation of the experimental parameters and their associated ID's.

Please note: Oxford University Press is not responsible for the content or functionality of any supporting materials supplied by the authors. Any queries (other than missing material) should be directed to the corresponding author for the article.

This paper has been typeset from a TEX/LATEX file prepared by the author.